Co_2FeAl thin films grown on MgO substrates: Correlation between static, dynamic, and structural properties

M. Belmeguenai,[1,*] H. Tuzcuoglu,[1] M. S. Gabor,[2,†] T. Petrisor, Jr.,[2] C. Tiusan,[2,3] D. Berling,[4] F. Zighem,[1] T. Chauveau,[1] S. M. Chérif,[1] and P. Moch[1]

[1]*LSPM (CNRS-UPR 3407), 99 avenue Jean-Baptiste Clément, Université Paris 13, 93430 Villetaneuse, France*

[2]*Center for Superconductivity, Spintronics and Surface Science, Technical University of Cluj-Napoca, 28 Memorandumului RO-400114 Cluj-Napoca, Romania*

[3]*Institut Jean Lamour, CNRS, Université de Nancy, BP 70239, F-54506 Vandoeuvre, France*

[4]*IS2M (CNRS-LRC 7228), 15 rue Jean Starcky, Université de Haute-Alsace, BP 2488, 68057 Mulhouse-Cedex, France*

(Received 20 December 2012; published 29 May 2013)

Co_2FeAl (CFA) thin films with thickness varying from 10 to 115 nm have been deposited on MgO(001) substrates by magnetron sputtering and then capped by a Ta or Cr layer. X-ray diffraction (XRD) revealed that the cubic [001] CFA axis is normal to the substrate and that all the CFA films exhibit full epitaxial growth. The chemical order varies from the B2 phase to the A2 phase when decreasing the thickness. Magneto-optical Kerr effect (MOKE) and vibrating sample magnetometer (VSM) measurements show that, depending on the field orientation, one- or two-step switchings occur. Moreover, the films present a quadratic MOKE signal increasing with the CFA thickness, due to the increasing chemical order. Ferromagnetic resonance (FMR), MOKE transverse bias initial inverse susceptibility and torque (TBIIST) measurements reveal that the in-plane anisotropy results from the superposition of a uniaxial and of a fourfold symmetry term. The fourfold anisotropy is in accord with the crystal structure of the samples and is correlated to the biaxial strain and to the chemical order present in the films. In addition, a large negative perpendicular uniaxial anisotropy is observed. Frequency and angular dependencies of the ferromagnetic resonance linewidth show two magnon scattering and mosaicity contributions, which depend on the CFA thickness. A Gilbert damping coefficient as low as 0.0011 is found.

DOI: 10.1103/PhysRevB.87.184431 PACS number(s): 76.50.+g, 75.40.Gb, 75.40.Cx, 75.70.Ak

I. INTRODUCTION

The performances of spintronic devices depend on the spin polarization of the current. Therefore, half metallic materials should be ideal compounds as high spin polarized current sources to realize a very large giant magnetoresistance, a low current density for current induced magnetization reversal, and an efficient spin injection into semiconductors. Theoretically, different kinds of materials, such as Fe_3O_4,[1,2] CrO_2,[3] mixed valence perovskites,[4] and Heusler alloys,[5,6] have been predicted to be half metals. Moreover, the half metallic properties in these materials have been experimentally demonstrated at low temperature. However, oxide half metals have low Curie temperature (T_C) and therefore their spin polarization is miserably low at room temperature. From this point of view, Heusler alloys are promising materials for spintronics applications, because a number of them have generally high T_C (Ref. 7) and therefore they may offer an alternative material choice to obtain half metallicity even at room temperature. Furthermore, their structural and electronic properties strongly depend on the crystal structure. Recently, Heusler compounds have attracted considerable experimental and theoretical interest, not only because of their half metallic behavior but also due to magnetic shape memory and inverse magnetocaloric properties that they exhibit.

One of the most important Co-based full-Heusler alloys is Co_2FeAl (CFA). It has a high T_C ($T_C = 1000$ K)[7] and, therefore, it is promising for practical applications. Indeed, it can provide giant tunneling magnetoresistance (360% at RT)[8,9] when used as an electrode in magnetic tunnel junctions. Furthermore, as we illustrate in our present study, CFA presents the lowest magnetic damping parameter among Heuslers. This low damping should provide significantly lower current density required for spin-transfer torque (STT) switching, particularly important in prospective STT devices. However, the integration of CFA as a ferromagnetic electrode in spintronic devices requires good knowledge, allowing for precise control, of its magnetic properties, such as its magnetization at saturation, its magnetic anisotropy, the exchange stiffness parameter, the gyromagnetic factor, and the damping mechanisms monitoring its dynamic behavior.

In this paper we used x-ray diffraction (XRD), ferromagnetic resonance in microstrip line (MS-FMR) under in-plane and out-of-plane applied magnetic fields, combined with transverse biased initial inverse susceptibility and torque (TBIIST) method, in order to perform a complete correlated analysis between structural and magnetic properties of epitaxial Co_2FeAl thin films grown on MgO(001) substrates. In addition, a detailed study of the different relaxation mechanisms leading to the linewidth broadening is presented.

II. SAMPLES PREPARATION AND EXPERIMENTAL METHODS

CFA films were grown on MgO(001) single-crystal substrates using a magnetron sputtering system with a base pressure lower than 3×10^{-9} Torr. Prior to the deposition of the CFA films, a 4 nm thick MgO buffer layer was grown at room temperature (RT) by rf sputtering from a MgO polycrystalline target under an argon pressure of 15 mTorr. Next, the CFA films, with variable thicknesses ($10 \leqslant d \leqslant 115$ nm), were deposited at RT by dc sputtering under an argon pressure

of 1 mTorr, at a rate of 0.1 nm/s. Finally, the CFA films were capped with a MgO(4 nm)/Cr(10 nm) or with a MgO (4 nm)/Ta(10 nm) bilayer. After the growth of the stack, the structures were *ex situ* annealed at 600 °C during 15 min in vacuum (pressure lower than 3×10^{-8} Torr).

The structural properties of the samples have been characterized by XRD using a four-circle diffractometer. Their magnetic dynamic properties have been studied by microstrip ferromagnetic resonance. The MS-FMR characterization was done with the help of a field modulated FMR setup using a vector network analyzer (VNA) operating in the 0.1–40 GHz frequency range. The sample (with the film side in direct contact) is mounted on a 0.5 mm microstrip line connected to the VNA and to a lock-in amplifier to derive the field modulated measurements via a Schottky detector. This setup is piloted via a Labview program providing flexibility of a real time control of the magnetic field-sweep direction, step and rate, real time data acquisition, and visualization. It allows both frequency and field-sweeps measurements with magnetic fields up to 20 kOe applied parallel or perpendicular to the sample plane. In-plane angular dependence of resonance frequencies and fields are used to measure anisotropies. The complete analysis of in-plane and perpendicular field resonance spectra exhibiting uniform precession and perpendicular standing spin wave (PSSW) modes leads to the determination of most of the magnetic parameters: effective magnetization, gyromagnetic factor, exchange stiffness constant, and anisotropy terms. In addition, the angular and the frequency dependencies of the FMR linewidth are used in order to identify the relaxation mechanisms responsible for the line broadening and allow us to evaluate the parameters which monitor the intrinsic damping (Gilbert constant) and the extrinsic one (two magnon scattering, inhomogeneity, mosaicity).

Magnetization at saturation and hysteresis loops for each sample were measured at room temperature using a vibrating sample magnetometer (VSM) and a magneto-optical Kerr effect (MOKE) system. TBIIST[10] has been used to study the in-plane anisotropy for comparison with MS-FMR. In this technique both a longitudinal magnetic sweep field $\boldsymbol{H_L}$ (parallel to the incidence plane) and a static transverse field $\boldsymbol{H_B}$ (perpendicular to the incidence plane) are applied in the plane of the film and the longitudinal reduced magnetization component m_L is measured versus H_L for various directions of $\boldsymbol{H_L}$ with conventional magneto-optical Kerr setup. From the measured hysteresis loops $m_L(H_L)$ under transverse biased field, the initial inverse susceptibility (χ^{-1}) and the field offset (δH) which are related to the second and first angle derivative of the magnetic anisotropy energy, respectively, are derived. Fourier analysis of χ^{-1} and δH versus the applied field direction then easily resolves contributions to the magnetic anisotropy of different orders and gives the precise corresponding values of their amplitude and of their principal axes.

In order to obtain the desirable accuracy or even simply meaningful results, higher-order nonlinear in m_L contributions (quadratic or Voigt effect) as well as polar or other contributions to the Kerr signal are carefully determined and corrected.[10] The TBIIST method surely does not have the same recognition as FMR techniques but seems to be complementary, especially for samples with a weak magnetic signal detectable with difficulty by FMR methods.

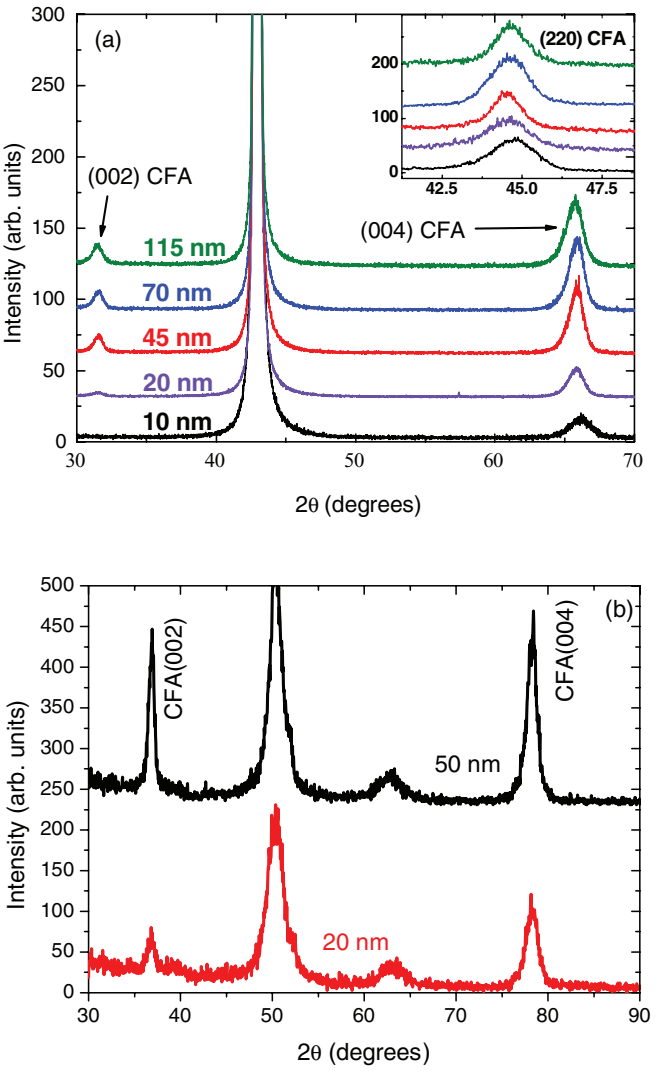

FIG. 1. (Color online) (a) X-ray 2θ-ω (out-of-plane) diffraction pattern using (Cu x-ray source) for the Cr-capped and (b) θ-2θ pattern (Co x-ray source) for the Ta-capped Co_2FeAl of different thicknesses. The inset shows selected area in plane diffraction patterns around (220) Co_2FeAl reflection.

III. STRUCTURAL CHARACTERIZATION

Figure 1 shows the x-ray 2θ-ω diffraction patterns for CFA of different thicknesses. These XRD patterns show that, in addition to the feature arising from the (002) peak of the MgO substrate, the Cr-capped samples [Fig. 1(a): Cu x-ray source ($\lambda = 0.154\,06$ nm)] exhibit only two peaks which are attributed to the (002) and (004) diffraction lines of CFA. The Ta-capped films [Fig. 1(b): Co x-ray source ($\lambda = 1.7902$ Å)] show an additional peak (around $2\theta = 63°$) arising from the (002) line issued from the Ta film. Pole figures (Fig. 2) allow us to assert an epitaxial growth of the CFA films according to the expected CFA(001)[110]//MgO(001)[100] epitaxial relation.

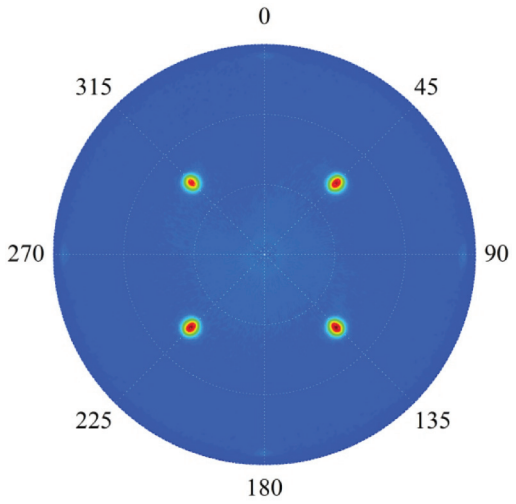

FIG. 2. (Color online) Pole figures around the Co_2FeAl (022) type reflection, for the 45 nm thick film, indicating the growth of Co_2FeAl on MgO with the Co_2FeAl (001)[110]//MgO(001)[100] epitaxial relation. The 0 and 90 deg axis of the graph correspond to the MgO [100] and [010] crystalline directions.

Using scans of various different orientations we evaluated the out-of-plane ($a_\perp$) and the in-plane ($a_\parallel$) lattice parameters (Fig. 3). A simple elastic model allowed us to derive the unstrained a_0 cubic parameter as well as the in-plane $\varepsilon_\parallel$ and the out-of-plane $\varepsilon_\perp$ strains:

$$a_0 = \frac{(C_{11}a_\perp + 2C_{12}a_\parallel)}{(C_{11}+2C_{12})}, \quad \varepsilon_\parallel = \frac{C_{11}}{(C_{11}+2C_{12})}\frac{(a_\parallel - a_\perp)}{a_0},$$
$$\varepsilon_\perp = -\frac{2C_{12}}{(C_{11}+2C_{12})}\frac{(a_\parallel - a_\perp)}{a_0}, \qquad (1)$$

where the values of the elastic constants $C_{11} = 253$ GPa and $C_{12} = 165$ GPa have been calculated previously.[11] Introducing the Poisson coefficient $\nu = C_{12}/(C_{11}+C_{12})$ the

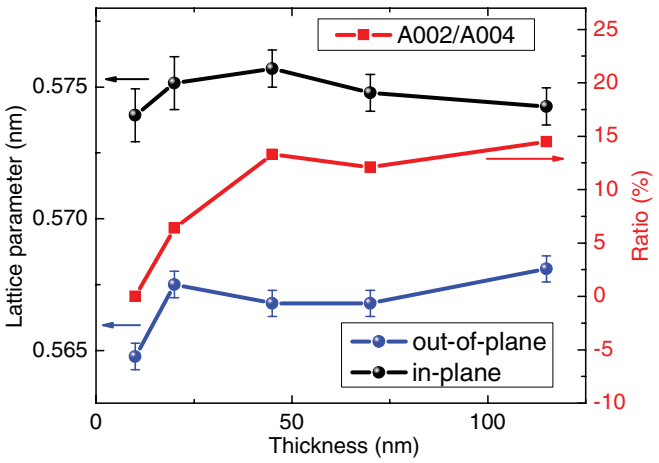

FIG. 3. (Color online) Evolution of the out-of-plane and in-plane lattice parameters and of the ratio of the integral intensities of the (002) and (004) Co_2FeAl peaks $A(002)/A(004)$ with respect to the Co_2FeAl films thickness.

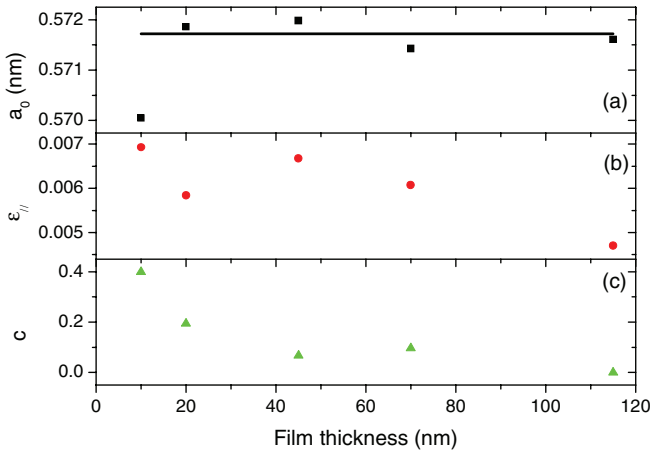

FIG. 4. (Color online) Thickness dependence of (a) the lattice cubic parameter a_0, the in-plane strain $\varepsilon_\parallel$, and (c) the chemical order c of Co_2FeAl thin films.

above parameters are:

$$a_0 = \frac{[(1-\nu)a_\perp + 2\nu a_\parallel]}{(1+\nu)}, \quad \varepsilon_\perp = \frac{(1-\nu)}{(1+\nu)}\frac{(a_\parallel - a_\perp)}{a_0},$$
$$\varepsilon_\parallel = -\frac{2\nu}{(1+\nu)}\frac{(a_\parallel - a_\perp)}{a_0}. \qquad (2)$$

The cubic lattice constant a_0 does not depend upon the thickness, except for the thinner 10 nm film [Fig. 4(a)], which shows a significant reduction; its value 0.5717 ± 0.0005 nm is slightly smaller than the reported one in the bulk compound with the $L2_1$ structure (0.574 nm). The in-plane strain $\varepsilon_\parallel$ reveals a tensile stress originating from the mismatch with the lattice of the MgO substrate: However, its value does not exceed a few ‰, well below the Heusler/MgO mismatch, thus excluding an efficient planar clamping. The strain $\varepsilon_\parallel$ decreases versus the thickness, at least above 40 nm [Fig. 4(b)].

Odd Miller indices [e.g., (111), (311),. . .] are allowed for diffraction in the $L2_1$ phase.[12] In contrast, they are forbidden in the B2 phase, which is characterized by a total disorder between Al and Fe atoms but a regular occupation of the Co sites. In the A2 phase the chemical disorder between Fe, Co, and Al sites is complete: (hkl) diffraction is only allowed for even indices subjected to $h + k + l = 4n$. We do not observe (111) or (311) lines and then conclude with the absence of the $L2_1$ phase in the studied films. In contrast, a (002) peak is observed, thus indicating that the samples do not belong to the A2 phase. However, the ratio I_{002}/I_{004} of the integrated intensities of the (002) and of the (004) peaks increases versus the film thickness (Fig. 3). This ratio is proportional to $(1-2c)^2$, where c is the chemical disorder. Assuming that the thickest film belongs to the B2 phase ($c = 0$), the dependence of c upon the film thickness is shown in Fig. 4(c): The A2 phase ($c = 0.5$) is almost completely achieved for the 10 nm thick sample. The reduction of a_0 in the thinner sample is probably due to its previously noticed[13] smaller value in the A2 phase compared to the B2 one.

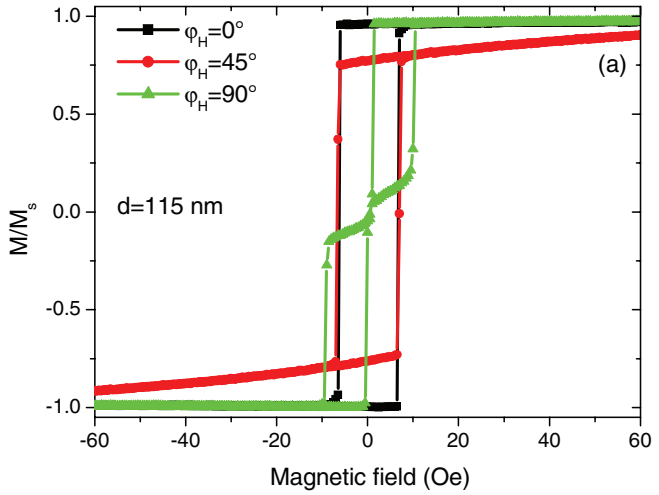

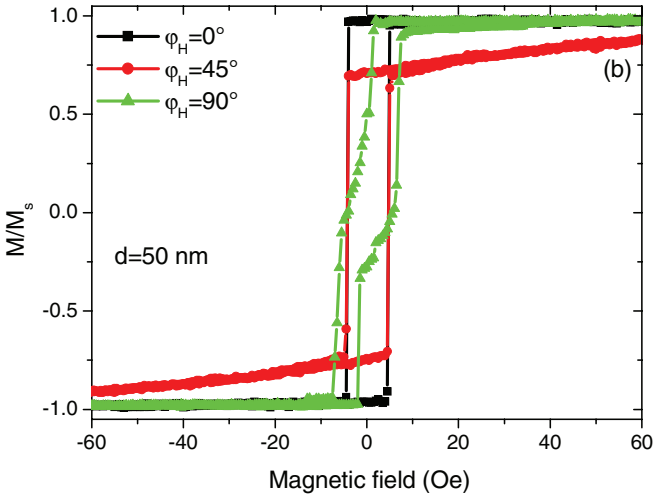

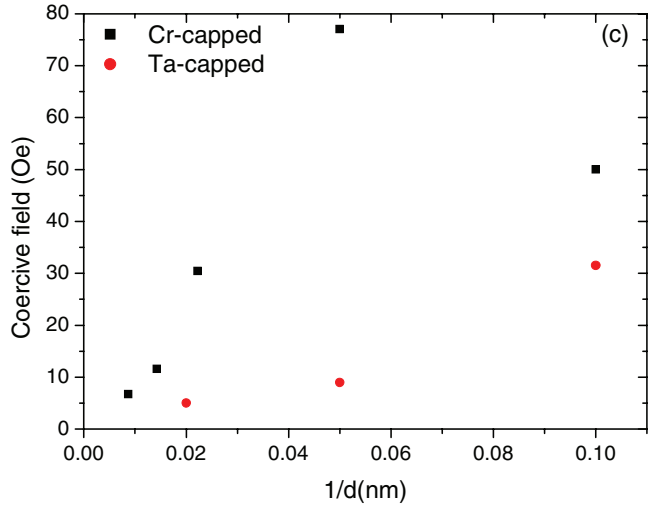

FIG. 5. (Color online) MOKE hysteresis loops of the (a) 115 nm Cr-capped and (b) 50 nm Ta-capped Co_2FeAl thin films. The magnetic field is applied parallel to the film surface, at various angles (φ_H) with respect to edges of the MgO substrate ([100] or [010]). (c) Thickness dependence of the coercive field, deduced from hysteresis loops along the easy axis, of Co_2FeAl Cr- and Ta-capped thin films.

IV. MAGNETIC PROPERTIES

The experimental magnetic data have been analyzed considering a magnetic energy density which, in addition to Zeeman, demagnetizing, and exchange terms, is characterized by the following effective anisotropy contribution:[14]

$$E_{\text{anis}} = -\tfrac{1}{2}[1+\cos 2(\varphi_M-\varphi_u)]K_u \sin^2\theta_M + K_\perp \sin^2\theta_M - \tfrac{1}{8}[3+\cos 4(\varphi_M-\varphi_4)]K_4 \sin^4\theta_M. \quad (3)$$

In the above expression, θ_M and φ_M, respectively, represent the out-of-plane and the in-plane (referring to the substrate edges) angles defining the direction of the magnetization $\boldsymbol{M}_s$. φ_u and φ_4 define the angles between an easy uniaxial planar axis or an easy planar fourfold axis, respectively, with respect to this substrate edge. K_u, K_4, and $K_\perp$ are in-plane uniaxial, fourfold, and out-of-plane uniaxial anisotropy constants, respectively. We introduce the effective magnetization $M_{\text{eff}} = H_{\text{eff}}/4\pi$ obtained by:

$$4\pi M_{\text{eff}} = H_{\text{eff}} = 4\pi M_s - \frac{2K_\perp}{M_s} = 4\pi M_s - H_\perp. \quad (4)$$

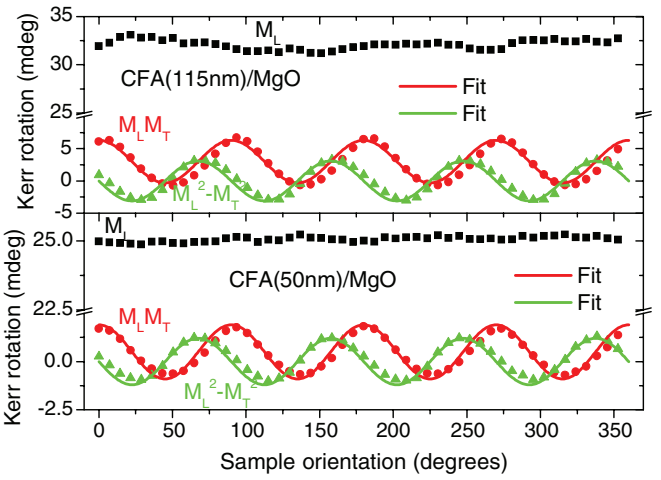

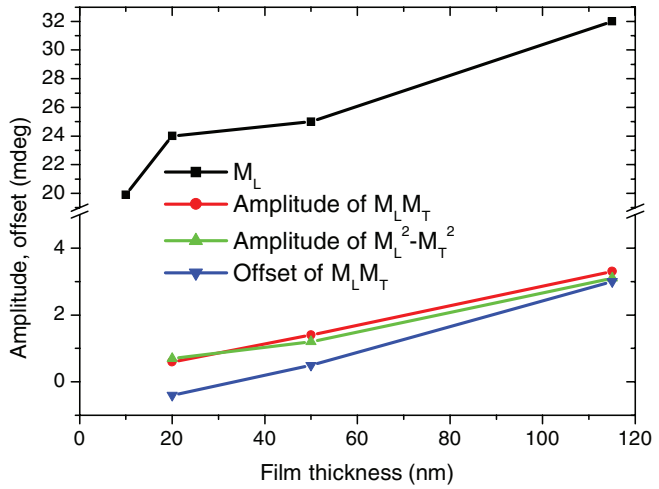

FIG. 6. (Color online) (a) Separated quadratic MOKE contributions as a function of the sample orientation at 46° incidence. The fits are obtained using Eq. (12). (b) The M_L contribution (at angle of incidence of 46°), the amplitudes and offset of the $M_L M_T$ contribution, and the amplitude of the $(M_L{}^2 - M_T{}^2)$ as a function of the Co_2FeAl thickness.

As experimentally observed, the effective perpendicular anisotropy term $K_\perp$ (and, consequently, the effective perpendicular anisotropy field $H_\perp$), is thickness dependent: $K_\perp$ describes an effective perpendicular anisotropy term

$$K_\perp = K_{\perp v} + 2K_{\perp s}/d, \tag{5}$$

where $K_{\perp s}$ refers to the perpendicular anisotropy term of the interfacial energy density. Finally we define $H_u = \frac{2K_u}{M_s}$ and $H_4 = \frac{4K_4}{M_s}$ as the in-plane uniaxial and the fourfold anisotropy fields, respectively.

The resonance expressions for the frequency of the uniform and PSSW modes assuming in-plane or perpendicular applied magnetic fields are given by Eqs. (6) and (7), respectively,[14,15]

$$F_n^2 = \left(\frac{\gamma}{2\pi}\right)^2 \left[H\cos(\varphi_H - \varphi_M) + \frac{2K_4}{M_s}\cos 4(\varphi_M - \varphi_4) + \frac{2K_u}{M_s}\cos 2(\varphi_M - \varphi_u) + \frac{2A_{\rm ex}}{M_s}\left(\frac{n\pi}{d}\right)^2\right]$$

$$\times \left\{H\cos(\varphi_H - \varphi_M) + 4\pi M_{\rm eff} + \frac{K_4}{2M_s}[3 + \cos 4(\varphi_M - \varphi_4)] + \frac{K_u}{M_s}[1 + \cos 2(\varphi_M - \varphi_u)] + \frac{2A_{\rm ex}}{M_s}\left(\frac{n\pi}{d}\right)^2\right\}, \tag{6}$$

$$F_\perp = \left(\frac{\gamma}{2\pi}\right)\left[H - 4\pi M_{\rm eff} + \frac{2A_{\rm ex}}{M_s}\left(\frac{n\pi}{d}\right)^2\right]. \tag{7}$$

In the above expressions $(\gamma/2\pi) = g \times 1.397 \times 10^6$ Hz/Oe is the gyromagnetic factor, n is the index of the PSSW, and $A_{\rm ex}$ is the exchange stiffness constant.

The experimental results concerning the measured peak-to-peak FMR linewidths $\Delta H^{\rm PP}$ are analyzed in this work taking account of both intrinsic and extrinsic mechanisms. Therefore, in most of the FMR experiments, the observed magnetic field linewidth ($\Delta H^{\rm PP}$) is usually analyzed by considering at least

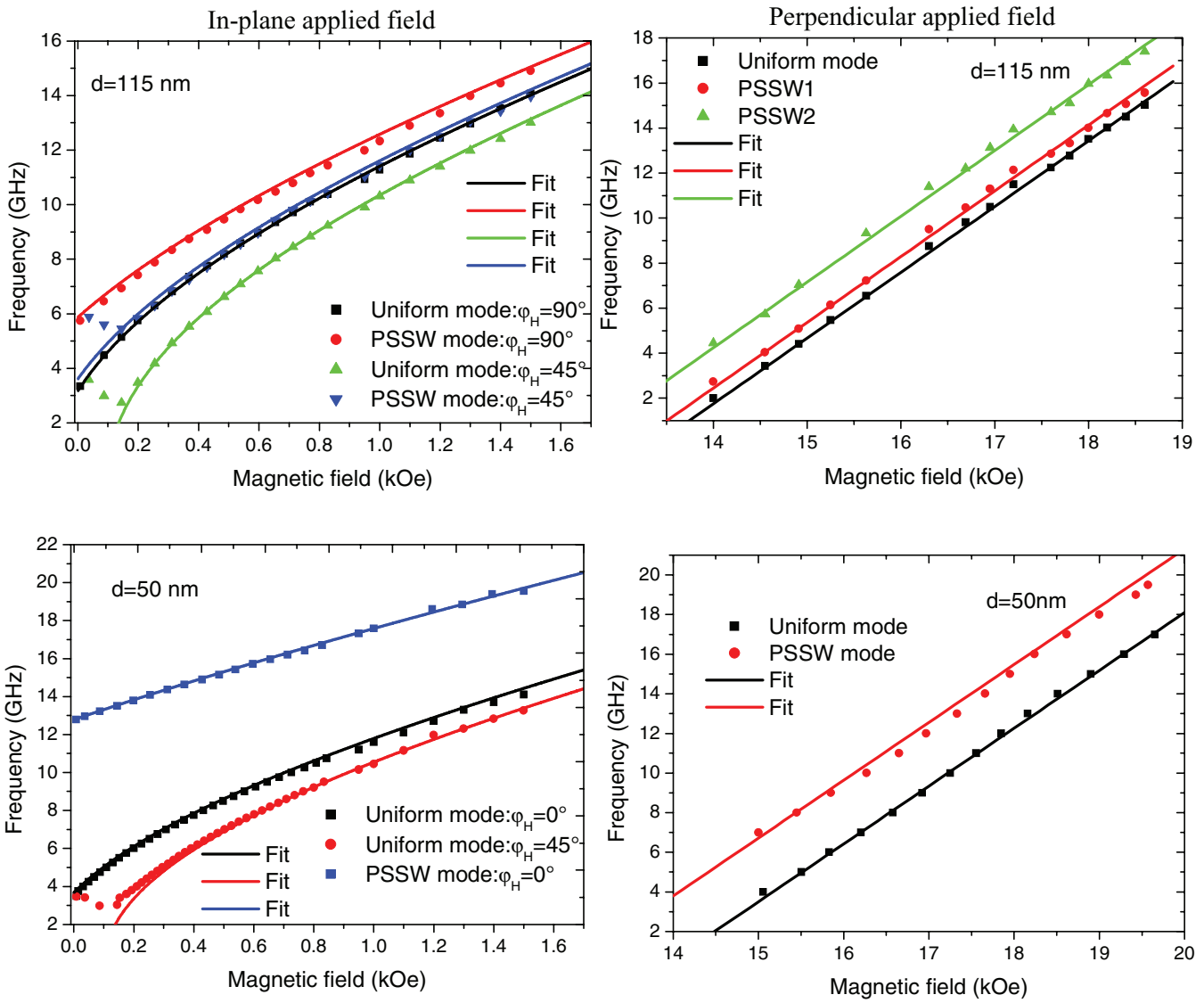

FIG. 7. (Color online) Field dependence of the resonance frequency of the uniform precession and of the two first perpendicular standing spin wave excited (PSSW) modes of 115 nm Cr-capped and 50 nm Ta-capped Co_2FeAl films. The magnetic field is applied perpendicular or in the film plane. The fits are obtained using Eqs. (6) and (7) with the parameters indicated in Table I.

four different contributions as given by Eq. (8),[16–21]

$$\Delta H^{\mathrm{PP}} = \Delta H^{\mathrm{Gi}} + (\Delta H^{\mathrm{mos}} + \Delta H^{\mathrm{inh}} + \Delta H^{\mathrm{2mag}}). \tag{8}$$

When the applied field and the magnetization are parallel, the intrinsic contribution is not angular dependent; it derives from the Gilbert damping and is given by:

$$\Delta H^{\mathrm{Gi}} = \frac{2}{\sqrt{3}}\frac{\alpha}{\gamma}2\pi f, \tag{9}$$

where f is the driven frequency and α is the Gilbert coefficient.

The relevant mechanisms[16] describing the extrinsic contributions are:

(1) The mosaicity: The orientation spread of the crystallites contributes to the linewidth. Its contribution is given by

$$\Delta H^{\mathrm{mos}} = \left|\frac{\partial H_{\mathrm{res}}}{\partial \varphi_H}\right| \Delta\varphi_H = \left|\frac{\partial H}{\partial \varphi_H}\right|_{\mathrm{res}} \Delta\varphi_H, \tag{10}$$

where $\Delta\varphi_H$ is the average spread of the easy axis anisotropy direction in the film plane. The suffix "res" indicates that Eq. (10) should be evaluated at the resonance. It is worth mentioning that along the easy and the hard axes the partial derivatives are zero and that, consequently, the mosaicity contribution vanishes. The expression of $\partial H/\partial\varphi_H$ is obtained from Eq. (6) for the uniform mode ($n = 0$), and subsequently calculated using the values of H and φ_M at the resonance.

(2) The inhomogeneous residual linewidth ΔH^{inh}. This contribution, which is frequency and angle independent, is related to various local fluctuations such as the value of the film thickness.

(3) Two magnon scattering contribution to the linewidth. This contribution is given by[22–24]

$$\Delta H^{\mathrm{2mag}} = [\Gamma_0 + \Gamma_2 \cos 2(\varphi_H - \varphi_2) + \Gamma_4 \cos 4(\varphi_H - \varphi_4)] \times \arcsin\left(\frac{f}{\sqrt{f^2 + f_0^2} + f_0}\right), \tag{11}$$

with $f_0 = \gamma M_{\mathrm{eff}}$. The expected fourfold symmetry induces the Γ_0 and Γ_4 coefficients; the coefficient Γ_2 is phenomenogically introduced.

The analysis of the variation of the resonance linewidth ΔH^{PP} versus the frequency and the in-plane field orientation allows for evaluating α, $\Delta\varphi_H$, ΔH^{inh}, Γ_0, Γ_2 (and φ_2), and Γ_4 (and φ_4 which, from symmetry considerations, is expected to have a 0° or 45° value, depending upon the chosen sign of Γ_4).

A. Static properties

The magnetization at saturation measured by VSM, averaged upon all the samples, has been found to be $M_s = 1000 \pm 50$ emu/cm^3, thus providing a magnetic moment of 5.05 ± 0.25 μ_B (Bohr magneton) per unit formula, in agreement with the previously published values for the B2 phase.[7]

For all the studied films the hysteresis loops were obtained by VSM and MOKE with an in-plane magnetic field applied along various orientations. Figure 5 shows representative behaviors of different CFA films. The observed shape mainly depends on the field orientation, in agreement with the expected characteristics of the magnetic anisotropy. As confirmed below, in all the studied samples, this anisotropy consists of the superposition of a fourfold and of a uniaxial term showing parallel easy axes. This common axis coincides with one of the substrate edges and, consequently, with one of the ⟨110⟩ crystallographic directions of the CFA phase. It results that if an orientation (say $\varphi_H = 0$ related to [110]) is the easiest, the perpendicular direction {($\varphi_H = 90°$) related to[1$\bar{1}$0]} is less easy. A similar situation was studied and interpreted previously[25]. It is expected to provide square hysteresis loops for $\varphi_H = 0$, while in contrast, for $\varphi_H = 90°$, it leads to a two steps reversal, as can be seen in Fig. 5. The intermediate step leads to a magnetization nearly perpendicular to the applied field. For all the studied films a two steps loop is observed for φ_H ranging in the {55°–130°}, interval. In Fig. 5(c) the deduced coercive fields (H_C) from hysteresis loops along the easy direction ($\varphi_H = 0$) are compared for different thicknesses (10, 20, 45, 50, 70, and 115 nm). For both Cr-capped and Ta-capped films, H_C increases linearly with the inverse of the film thickness. The Cr-capped samples present higher coercive fields due to the different interface quality.

One can also observe that MOKE hysteresis loops are not strictly centrosymmetrical [see for example Fig. 5(b) for $\varphi_H = 90°$] indicating the superposition of symmetrical (even function of applied sweep field H_L) and antisymmetrical (odd in H_L) components in the Kerr signal. It has been shown and confirmed[26,27] that, for in-plane magnetized thin films, the antisymmetrical part observed in the $m_L(H_L)$ loops arises from the second order magneto-optical effects quadratic in magnetization. Therefore, the present study was not limited to the usual linear MOKE. We have also investigated this quadratic contribution through the study of the Kerr signal dependence upon the film orientation under a saturating in-plane field. Within the cubic approximation for a (001) surface, the Kerr rotation angle is:[27]

$$\theta_K = a_1 M_L + a_2\left(M_L^2 - M_T^2\right)\sin[4\psi] + (b_2 + 2a_2\cos[4\psi])M_L M_T, \tag{12}$$

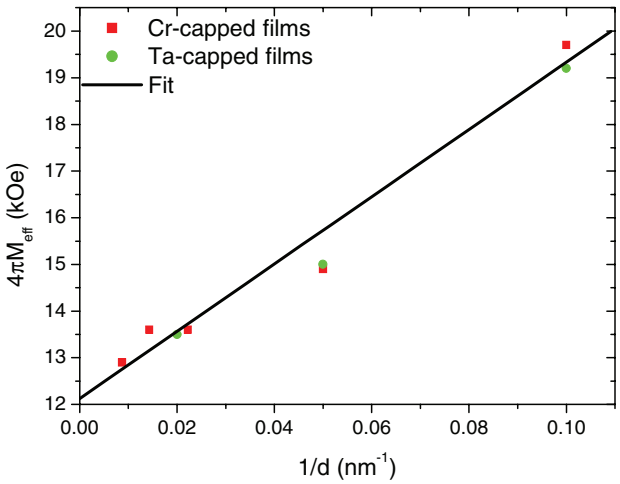

FIG. 8. (Color online) Thickness dependence of the effective magnetization ($4\pi M_{\mathrm{eff}}$) extracted from the fit of FMR measurements. The solid lines are the linear fits.

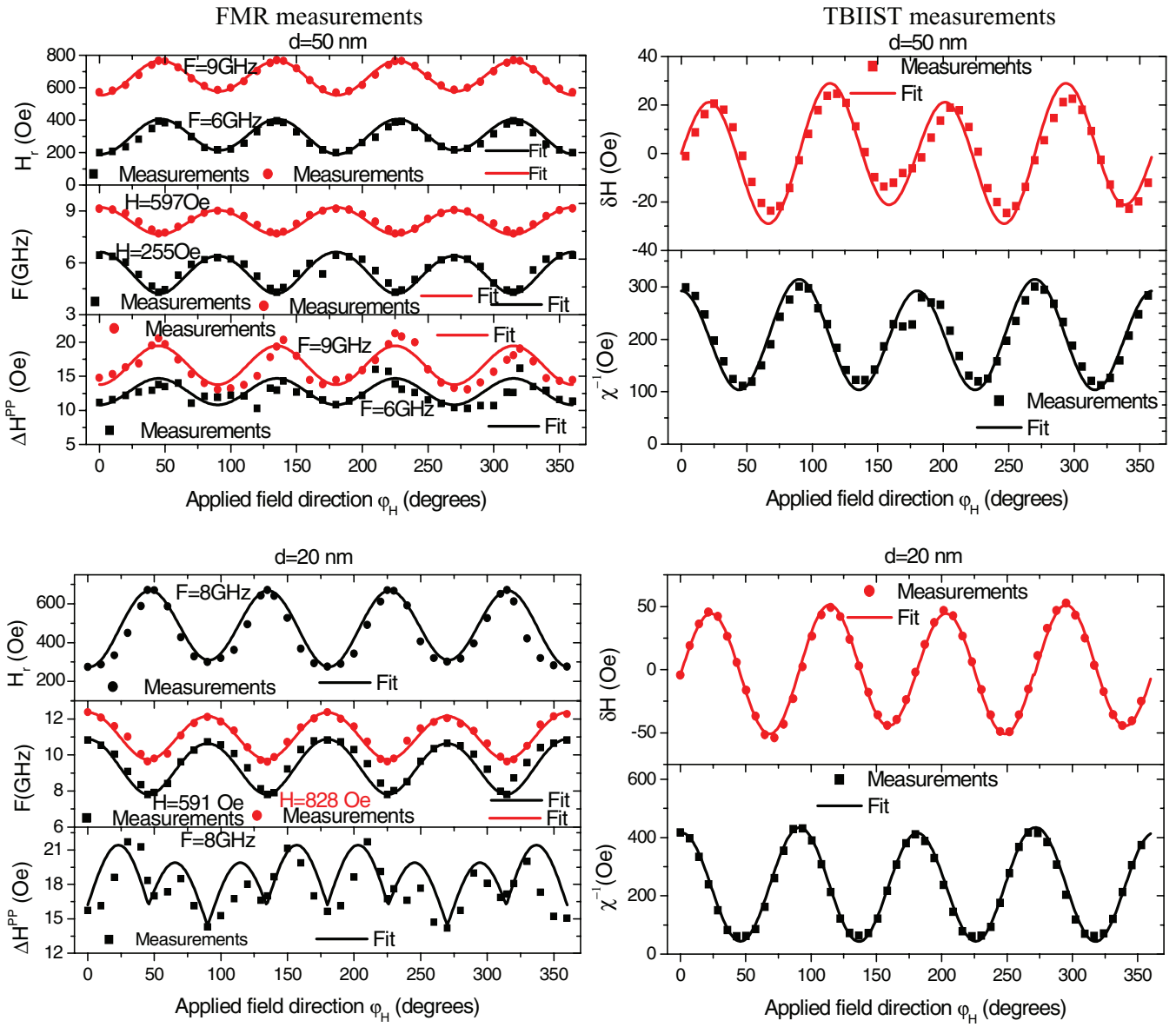

FIG. 9. (Color online) Angular dependence of the resonance frequency (F), resonance field (H_r), peak to peak field FMR linewidth (ΔH^{PP}), inverse susceptibility (χ^{-1}), and the field offset (δH) of 50 and 20 nm thick Co_2FeAl Ta-capped thin films. The TBIIST measurements were obtained using transverse static bias field $H_B = 200$ and 225 Oe, respectively, for 50 and 20 nm thick Co_2FeAl films. The solid lines refer to the fit using the above-mentioned models.

where M_L and M_T stand for the longitudinal (i.e., within the incidence plane) and the transverse (i.e., normal to the incidence plane) component of the magnetization, respectively, and where ψ is the angle of a cubic $\langle 110 \rangle$ axis with the plane of incidence. The first term describes the usual linear contribution while the following ones correspond to the quadratic MOKE (QMOKE). The experimental study was performed under an angle of incidence of 46° using a large field magnitude with respect to the anisotropy field. The different contributions to the Kerr signal, as functions of the film orientation ψ, are extracted by applying a rotating field technique.[10] Representative results obtained with 115 Cr- and 50 nm Ta-capped films are shown in Fig. 6. Beside the longitudinal component (M_L) of the Kerr rotation, which is dominant, the QMOKE signal, which is most probably due to the second order spin-orbit coupling,[26] is present. The derived $({M_L}^2 - {M_T}^2)$ and $M_L M_T$ angular variations show the behavior expected from the above equation.

The values for the amplitudes of the $2M_L M_T$ and of the $({M_L}^2 - {M_T}^2)$ contributions are the same within the experimental error for each sample, suggesting that the applied cubic model is correct. The offset of the $M_L M_T$ contribution is smaller than the amplitudes, but generally it follows the same trend as the amplitudes. As the thickness decreases the amplitudes and the offset decrease, suggesting that the chemical order progressively changes from the B2 to the A2

phase, as discussed above. Moreover, the amplitudes and offset values of CFA are comparable to those measured for Co_2MnSi, which presents the $L2_1$ phase.[28]

The TBIIST results are discussed in the following section in order to allow for a comparison with the data derived from the FMR study of the dynamic properties.

B. Dynamic properties

1. Exchange stiffness and effective magnetization

The uniform precession and the first PSSW modes have been observed in perpendicular and in-plane applied field configurations for samples thicknesses down to 50 nm. For the thickest film (115 nm) it was even possible to observe the second PSSW. For lower sample thickness, the PSSW modes are not detected due their high frequencies over-passing the available bandwidth (0–24 GHz). Typical in-plane and perpendicular field dependencies of the resonance frequencies of the uniform and PSSW modes are shown in Fig. 7 for the 115 nm Cr- and the 50 nm Ta-capped films. By fitting the data in Fig. 7 to the above presented model, the gyromagnetic factor (γ), the exchange stiffness constant (A_{ex}), and the effective magnetization ($4\pi M_{eff}$) are extracted. The fitted γ and A_{ex} values are 2.92 GHz/kOe and 1.5 μerg/cm, respectively: They do not depend of the studied sample. The derived exchange constant is in good agreement with the reported one by Trudel *et al.*.[7]

Figure 8 plots out the extracted effective magnetization $4\pi M_{eff}$ versus the film thickness $1/d$. It can be seen that M_{eff} follows a linear variation. This allows us to derive the perpendicular surface anisotropy coefficient $K_{\perp s}$: $K_{\perp s} = -1.8$ erg/cm^2. The limit of $4\pi M_{eff}$ when $1/d$ tends to zero is equal to 12.2 kOe: Within the above mentioned experimental precision about the magnetization at saturation, it does not differ from $4\pi M_s$. We conclude that the perpendicular anisotropy field derives from a surface energy term; being negative, it provides an in-plane contribution. It may originate from the magnetoelastic coupling arising from the interfacial stress due to the substrate.

2. Magnetic anisotropy

Figure 9 shows the angular dependencies of the resonance field (at fixed frequency) and of the resonance frequency (at fixed applied field) compared to the static TBIIST measurements for three different CFA films. Both FMR and TBIIST data show that the angular behavior is governed by a superposition of uniaxial and fourfold anisotropy terms with the above mentioned easy axes. As noticed above, the symmetry properties of the epitaxial observed films agree with the principal directions of the fourfold contribution. The fourfold and uniaxial anisotropy fields extracted from the fit of the experimental TBIIST and FMR data using the above presented model are drawn in Fig. 10 and summarized in Table I: The compared results issued from the two techniques are in excellent agreement. For all the samples, the fourfold anisotropy is dominant. While the uniaxial anisotropy field (H_u) of the Cr-capped films is small and does not seem to depend upon the thickness, in the Ta-capped films H_u is higher, may be due to interface effects, and is a decreasing function of the thickness (Fig. 10). As suggested previously, we believe that the uniaxial anisotropy is induced by the stepping of the substrates, probably resulting from a small miscut along their

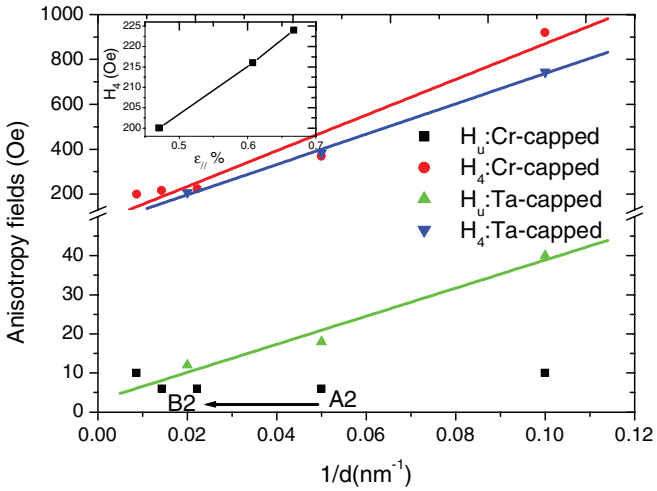

FIG. 10. (Color online) Thickness dependence of the uniaxial (H_u) and the fourfold anisotropy fields (H_4) extracted from the fit of FMR measurements. The solid lines are the linear fits. The inset shows the evolution of the H_4 field, for the 45, 70, and 115 nm thick samples, with the in-plane biaxial strain.

TABLE I. Magnetic parameters obtained from the best fits to our experimental FMR results with the above mentioned model. nd: not detected, nm: not measured.

	H_u (Oe)		H_4 (Oe)		φ_u (deg)		φ_4 (deg)				
d (nm)	FMR	TBIIST	FMR	TBIIST	FMR	TBIIST	FMR	TBIIST	$4\pi M_{eff}$ (kOe)	$\gamma/2\pi$ (GHz/kOe)	A_{ex} (μerg/cm)
						Cr-capped films					
115	10	9.5	200	200.5	0	0	0	0	12.9	2.92	1.45
70	6	12	216	202	0	0	0	0	13.6	2.92	1.5
45	6	10	224	201	0	0	0	0	13.6	2.92	1.5
20	6	7	368	375	0	0	0	0	14.8	2.92	nd
10	10	nm	920	nm	0	nm	0	nm	19.7	2.92	nd
						Ta-capped films					
50	12	11	208	200	0	0	0	0	13.5	2.92	1.5
20	18	18.5	384	376	0	0	0	1.3	15	2.92	nd
10	40	38	744	776	0	0	0	0	19.2	2.92	nd

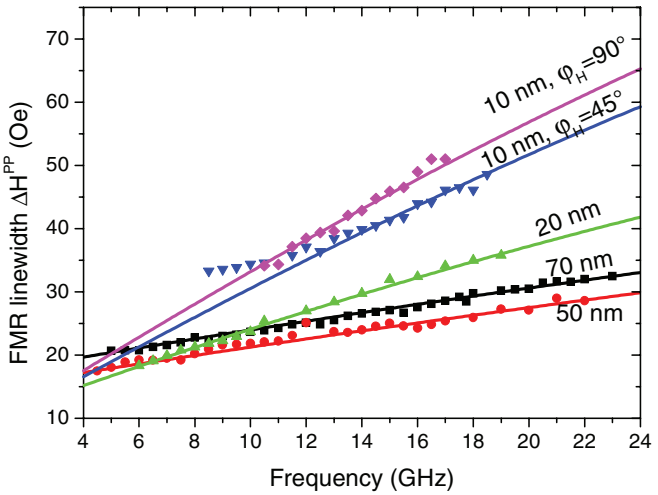

FIG. 11. (Color online) Frequency dependence of the easy axis ($\varphi_H = 0°$) peak to peak field FMR linewidth (ΔH^{PP}) for Co_2FeAl thin films. The solid lines refer to the fit using Eqs. (8)–(11).

[100] crystallographic direction corresponding to the [110] studied films. The reduced effect of the steps of the substrate when the thickness increases could then explain the thickness dependence of H_u. However, up to now we have no completely satisfying interpretation of the presence of H_u and of its variations versus the nature of the film capping.

The fourfold anisotropy fields (H_4) are comparable for Cr- and Ta-capped films and decrease when their thickness increases, as seen in Fig. 10. For large values of d (45 nm or higher) H_4 lies around 200 Oe and shows a small linear variation versus the in-plane strain $\varepsilon_{\parallel}$, as shown in the inset of Fig. 10. This evolution confirms a direct correlation between the H_4 field and the in-plane biaxial strain for the films with thicknesses above 45 nm. At smaller values of d (10 or 20 nm) a large increase of H_4, up to 920 Oe, is observed. It is presumably related to the B2 $\Rightarrow$ A2 phase transition observed through x-ray diffraction. The observed symmetry argues for a magnetocrystalline contribution, which, as previously observed,[29,30] would be higher in phase A2 than in phase B2.

3. *FMR linewidth*

In Fig. 9 the FMR peak to peak linewidth (ΔH^{PP}) is plotted as a function of the field angle φ_H for the 50 and 20 nm Ta-capped CFA films using three driving frequencies: 6, 8, and 9 GHz. ΔH^{PP} is defined as the field difference between the extrema of the sweep-field measured FMR spectra. All the other samples show a qualitatively similar behavior to one of the samples presented here. The positions of the extrema depend on the sample. The observed pronounced anisotropy of the linewidth cannot be due to the Gilbert damping contribution, which is expected to be isotropic, and must be due to additional extrinsic damping mechanisms. In the 50 nm thick sample, the ΔH^{PP} angular variation shows a perfect fourfold symmetry (in agreement with the variation of the resonance position). Such behavior is characteristic of two magnon scattering. This effect is correlated to the presence of defects preferentially oriented along specific crystallographic directions, thus leading to an asymmetry [see Eq. (11)]. Concerning the 20 nm thick film, the in-plane angular dependence of ΔH^{PP} is less simple and shows eight minima, as expected from a mosaicity driven linewidth broadening. It can be seen that a smaller fourfold symmetry contribution (four minima) is superimposed to this dominant behavior, indicating that two magnon scattering is still present. Therefore, the whole angular dependence of the FMR linewidth in our samples can be explained as a result of the four contributions appearing in Eq. (8).

In Fig. 11 ΔH^{PP} using applied fields parallel to an easy axis and to a hard axis ($\varphi_H = 45°$ for 10 nm thick sample) of the fourfold anisotropy is plotted as a function of driving frequency for all samples. Apparently an increase of the linewidth can be observed with decreasing film thickness. It should be mentioned that the observed linear increase of the linewidth with frequency in Fig. 11 results not only from Gilbert damping but, in addition, from other relaxation mechanisms. Anyway, an effective damping parameter α_{eff} can be extracted from the slope of the curves: it ranges between about 0.00154 for the easy axis of the 50 nm thick film and 0.0068 for easy axis of the thinnest film. The pertinent parameters could thus be, in principle, derived from the conjoint analysis of the frequency and angular dependence of ΔH^{PP}. However, due to the limited experimental precision, some additional hypotheses are necessary in order to allow for a complete determination of the whole set of parameters describing the intrinsic Gilbert damping and the two magnon damping. A detailed analysis is presented in the Appendix assuming $\alpha = 1.1 \times 10^{-3}$,[31] which is in agreement with our experimental results, we were thus able to evaluate for each film Γ_0, Γ_2, Γ_4, φ_2, φ_4. They are listed in Table II, which also contains the parameters describing the damping effects of the mosaïcity ($\Delta\varphi_H$) and of the inhomogeneity contribution (ΔH^{inh}).

The two magnon and the mosaicity ($\Delta\varphi_H$) contributions to ΔH^{PP} increase when the thickness decreases, probably due to the progressive loss of chemical order reported above. The increase of the residual inhomogeneities linewidth (ΔH^{inh}) with the thickness is most probably due to the increase of defects and roughness. The uniaxial term Γ_2 is observed only

TABLE II. Magnetic parameters obtained from the best fits to our data of angular and frequency dependencies of the peak to peak FMR linewidth. np: not pertinent. The mosaicity and the residual inhomogeneities linewidth contributions are given by $\Delta\varphi_H$ and ΔH^{inh}, respectively.

d (nm)	Cap layer	α	ΔH^{inh} (Oe)	$\Delta\varphi_H$ (deg)	Γ_0 (Oe)	Γ_2 (Oe)	Γ_4 (Oe)	φ_2 (deg)	φ_4 (deg)
70	Cr	1.1×10^{-3}	16.8	0.17	7.5	0	2.5	np	0
50	Ta	1.1×10^{-3}	14.5		24	0	−14	np	0
20	Ta	1.1×10^{-3}	7	0.37	49.5	5	−2.5	0	0
10	Ta	1.1×10^{-3}	6.5	0.51	124	3.5	12.5	0	0

in the thinnest (20 and 10 nm) samples. As expected, $\varphi_4 = 0$, but the sign of Γ_4 is sample dependent. Finally, it is important to notice that the very low value of the intrinsic damping in the studied samples allows for investigating the extrinsic contributions.

V. CONCLUSION

Co_2FeAl films of various thicknesses ($10 \leqslant d \leqslant 115$ nm) were prepared by sputtering on a (001) MgO substrate. They show full epitaxial growth with chemical order changing from B2 to A2 phase as thickness decreases. MOKE and VSM hysteresis loops obtained with different field orientations revealed that, depending on the direction of the in-plane applied field, two or one jump switchings occur, due to the superposition of uniaxial and fourfold anisotropies. The samples present a quadratic MOKE contribution with decreasing amplitudes as the CFA thickness decreases. The microstrip ferromagnetic resonance (MS-FMR) and the transverse biased initial inverse susceptibility and torque (TBIIST) methods have been used to study the dynamic properties and the anisotropy. The in-plane anisotropy presents two contributions, showing a fourfold and a twofold axial symmetry, respectively. Good agreement concerning the relevant in-plane anisotropy parameters deduced from the fit of MS-FMR and TBIIST measurements has been obtained. The fourfold in-plane field shows a thickness dependence behavior correlated to the thickness dependence of the chemical order and strain in samples. The angular and frequency dependencies of the FMR linewidth are governed by two magnon scattering, mosaïcity, and by a sample independent Gilbert damping equal to 0.0011.

ACKNOWLEDGMENTS

This work was partially supported by POS CCE Project ID.574, code SMIS-CSNR 12467 and CNCSIS UEFISCSU Project No PNII IDEI 4/2010 code ID-106.

APPENDIX

In the section dealing with the discussion of the FMR linewidth measurements we stated that the conjoint analysis of the frequency and of the angular dependencies of ΔH^{PP} does not allow for the determination of all the parameters appearing in Eq. (8) and that an additional hypothesis should be done. The aim of this Appendix is to clarify how the parameters summarized in Table II are derived.

For most of the exploitable measurements the microwave frequency f during the ΔH^{PP} measurements is not larger than f_0 and generally smaller (f_0 varies from 18.5 to 28.5 GHz, depending on the film thickness). It then results that the two magnon damping is practically proportional to f and that the sum of the Gilbert and of the two magnon damping terms reads as [see Eqs. (9) and (11)]:

$$\Delta H^{\mathrm{Gi+2mag}} \cong \left[\left(\frac{\alpha}{\sqrt{3}} + \frac{\Gamma_0}{2H_{\mathrm{eff}}} \right) + \frac{\Gamma_2}{2H_{\mathrm{eff}}} \cos 2(\varphi_H - \varphi_2) + \frac{\Gamma_4}{2H_{\mathrm{eff}}} \cos 4(\varphi_H - \varphi_4) \right] \frac{4\pi}{\gamma} f. \quad \text{(A1)}$$

It is not possible to completely identify the respective contributions of the Gilbert and of the two magnon damping, only according to Eq. (A1). The quasilinear variation versus the frequency (Fig. 11) observed for ΔH^{PP} allows for defining an effective damping parameter α_{eff}, which is angle dependent due to two magnon scattering. The experimentally derived coefficient α_{eff}, from the linear fit of data presented in Fig. 11, varies from 0.0068 to 0.00154. Furthermore, the measured angular variation of the linewidth allows for evaluating (Γ_2, φ_2) and (Γ_4, φ_4) but, concerning the isotropic terms appearing in Eq. (A1), only the sum $(\alpha + \frac{\sqrt{3}\Gamma_0}{2H_{\mathrm{eff}}})$ can be derived. However, remembering that α cannot be negative, the maximal available value of Γ_0 (corresponding to $\alpha = 0$) is easily found. Moreover, a lowest value can be obtained for Γ_0 noticing that Eq. (A1) can also be written:

$$\Delta H^{\mathrm{Gi+2mag}} \cong \left\{ \left(\frac{\alpha}{\sqrt{3}} + \frac{\Gamma_0 - |\Gamma_2| - |\Gamma_4|}{2H_{\mathrm{eff}}} \right) + \frac{|\Gamma_2|}{2H_{\mathrm{eff}}} [1 \pm \cos 2(\varphi_H - \varphi_2)] + \frac{|\Gamma_4|}{2H_{\mathrm{eff}}} [1 \pm \cos 4(\varphi_H - \varphi_4)] \right\} \frac{4\pi}{\gamma} f,$$

where the adequate third and the fourth terms represent the twofold and the fourfold contributions, which put in evidence that both of them are necessarily non-negative for any value of φ_H. The additional residual two magnon isotropic contribution cannot be negative. Hence $\Gamma_0 > |\Gamma_2| + |\Gamma_4|$.

Introducing this minimal accessible value of Γ_0 ($|\Gamma_2| + |\Gamma_4|$), the maximal value of the Gilbert coefficient α is then easily obtained. To summarize, for each sample the experimental data provide the allowed intervals for α and for Γ_0, respectively $[0, \alpha_{\min}]$ and $[(|\Gamma_2| + |\Gamma_4|), \Gamma_{0\max}]$, and indeed, the chosen value of α within $[0, \alpha_{\min}]$ allows for deducing Γ_0. The smallest calculated interval for α, equal to $[0, 1.4 \times 10^{-3}]$, is obtained for the 70 nm film. A previous publication by Mizukami *et al.*[31] has concluded to a Gilbert coefficient equal to $\alpha = 1.1 \times 10^{-3}$. We then stated that $\alpha = 1.1 \times 10^{-3}$ and, consequently, we were able to deduce Γ_0 for each film. Γ_0, Γ_2, Γ_4, φ_2, φ_4 are listed in Table II, which also contains the parameters describing the damping effects of the mosaicity and of the inhomogeneity.

*belmeguenai.mohamed@univ-paris13.fr
†mihai.gabor@phys.utcluj.ro

[1] A. Yanase and K. Siratori, J. Phys. Soc. Jpn. **53**, 312 (1984).
[2] Z. Zhang and S. Satpathy, Phys. Rev. B **44**, 13319 (1991).
[3] K. Schwarz, J. Phys. F **16**, L211 (1986).
[4] J. H. Park, E. Vescovo, H. J. Kim, C. Kwon, R. Ramesh, and T. Venkatesan, Nature (London) **392**, 794 (1998).
[5] H. C. Kandpal, G. H. Fecher, and C. Felser, J. Phys. D **40**, 1507 (2007).
[6] R. A. de Groot, F. M. Mueller, P. G. van Engen, and K. H. J. Buschow, Phys. Rev. Lett. **50**, 2024 (1983).

[7]S. Trudel, O. Gaier, J. Hamrle, and B. Hillebrands, J. Phys. D **43**, 193001 (2010).
[8]W. H. Wang, E. Liu, M. Kodzuka, H. Sukegawa, M. Wojcik, E. Jedryka, G. H. Wu, K. Inomata, S. Mitani, and K. Hono, Phys. Rev. B **81**, 140402(R) (2010).
[9]W. H. Wang, H. Sukegawa, and K. Inomata, Phys. Rev. B **82**, 092402 (2010).
[10]D. Berling, S. Zabrocki, R. Stephan, G. Garreau, J. L. Bubendorff, A. Mehdaoui, D. Bolmont, P. Wetzel, C. Pirri, and G. Gewinner, J. Magn. Magn. Mater. **297**, 118 (2006).
[11]M. S. Gabor, T. Petrisor Jr., C. Tiusan, M. Hehn, and T. Petrisor, Phys. Rev. B **84**, 134413 (2011).
[12]D. Fruchart, R. Fruchart, Ph. L'Héritier, K. Kanematsu, R. Madar, S. Misawa, Y. Nakamura, P. J. Ziebeck, and K. R. A. Webster, in *Magnetic Properties of Metals*, edited by H. P. J. Wijn, Landolt-Börnstein, New Series, Group III, Vol. 19c, Pt. 2 (Springer, Berlin, 1986).
[13]K. Inomata, N. Ikeda, N. Tezuk, R. Goto, S. Sugimoto, M. Wojcik, and E. Jedryka, Sci. Technol. Adv. Mater. **9**, 014101 (2008).
[14]M. Belmeguenai, F. Zighem, Y. Roussigné, S.-M. Chérif, P. Moch, K. Westerholt, G. Woltersdorf, and G. Bayreuther, Phys. Rev. B **79**, 024419 (2009).
[15]M. Belmeguenai, F. Zighem, T. Chauveau, D. Faurie, Y. Roussigné, S.-M. Chérif, P. Moch, K. Westerholt, and P. Monod, J. Appl. Phys. **108**, 063926 (2010).
[16]K. Zakeri, J. Lindner, I. Barsukov, R. Meckenstock, M. Farle, U. von Hörsten, H. Wende, W. Keune, J. Rocker, S. S. Kalarickal, K. Lenz, W. Kuch, K. Baberschke, and Z. Frait, Phys. Rev. B **76**, 104416 (2007).
[17]H. Lee, Y.-H. A. Wang, C. K. A. Mewes, W. H. Butler, T. Mewes, S. Maat, B. York, M. J. Carey, and J. R. Childress, Appl. Phys. Lett. **95**, 082502 (2009).
[18]H. Kurebayashi, T. D. Skinner, K. Khazen, K. Olejnik, D. Fang, C. Ciccarelli, R. P. Campion, B. L. Gallagher, L. Fleet, A. Hirohata, and A. J. Ferguson, Appl. Phys. Lett. **102**, 062415 (2013).
[19]K. D. Sossmeier, F. Beck, R. C. Gomes, L. F. Schelp, and M. Carara, J. Phys. D **43**, 055003 (2010).
[20]Y. Y. Zhou, X. Liu, J. K. Furdyna, M. A. Scarpulla, and O. D. Dubon, Phys. Rev. B **80**, 224403 (2009).
[21]W. Platow, A. N. Anisimov, G. L. Dunifer, M. Farle, and K. Baberschke, Phys. Rev. B **58**, 5611 (1998).
[22]R. Arias and D. L. Mills, Phys. Rev. B **60**, 7395 (1999).
[23]D. L. Mills and R. Arias, Physica B **384**, 147 (2006).
[24]R. Arias and D. L. Mills, J. Appl. Phys. **87**, 5455 (2000).
[25]R. P. Cowburn, S. J. Gray, J. Ferré, J. A. C. Bland, and J. Miltat, J. Appl. Phys. **78**, 7210 (1995).
[26]K. Postava, D. Hrabovsky, J. Pistora, A. R. Fert, S. Visnovsky, and T. Yamaguchi, J. Appl. Phys. **91**, 7293 (2002).
[27]R. M. Osgood III, S. D. Bader, B. M. Clemens, R. L. White, and H. Matsuyama, J. Magn. Magn. Mater. **182**, 297 (1998).
[28]G. Wolf, J. Hamrle, S. Trudel, T. Kubota, Y. Ando, and B. Hillebrands, J. Appl. Phys. **110**, 043904 (2011).
[29]O. Gaier, J. Hamrle, S. J. Hermsdoerfer, H. Schultheiß, B. Hillebrands, Y. Sakuraba, M. Oogane, and Y. Ando, J. Appl. Phys. **103**, 103910 (2008).
[30]S. Trudel, G. Wolf, J. Hamrle, B. Hillebrands, P. Klaer, M. Kallmayer, H.-J. Elmers, H. Sukegawa, W. Wang, and K. Inomata, Phys. Rev. B **83**, 104412 (2011).
[31]S. Mizukami, D. Watanabe, M. Oogane, Y. Ando, Y. Miura, M. Shirai, and T. Miyazaki, J. Appl. Phys. **105**, 07D306 (2009).